Article:

Ozdemir, B., Valdastri, P. and Chandler, J.H. (2026) Spring-Based Tendon-Driven Continuum Robots for Compact Modular Designs in Endoluminal Applications. IEEE/ASME Transactions on Mechatronics. ISSN: 1083-4435

https://doi.org/10.1109/tmech.2026.3694222

This article has been accepted for publication in IEEE/ASME Transactions on Mechatronics. This is the author's version which has not been fully edited and content may change prior to final publication. Citation information: DOI 10.1109/TMECH.2026.3694222

Spring-Based Tendon-Driven Continuum Robots for Compact Modular Designs in Endoluminal Applications

Burak Ozdemir, *Student Member, IEEE*, Pietro Valdastri, *Fellow, IEEE*, James H. Chandler, *Member, IEEE*

***Abstract*—Continuum robots have gained significant attention for endoluminal deployment due to their ability to operate in constrained environments. However, the complexity of many continuum robotic design approaches creates challenges in adapting robot geometry, dexterity, stiffness distribution, and functional integration to the requirements of specific medical procedures and/or patient-specific anatomy. This paper presents a modular and adaptable design approach for development of compact, multi-segment tendon-driven continuum robots. The design strategy employs a compliant helical spring backbone with inner and outer self-anchoring spacer disks, enabling simple reconfiguration of segments and actuation tendons without increased manufacturing complexity. A design framework is introduced to formalize disk–spring integration, and a two-segment, seven-tendon example is presented for robotically assisted bronchoscopy. The design achieves a minimum diameter of 4.2 mm with a 2.4 mm working channel housing a camera and biopsy tool. An adapted piecewise constant curvature model is presented to predict shape and tip pose, with a mean tip error of 4.0 mm. Navigation trials within a bronchial phantom reached predefined targets for biopsy needle deployment with an average positioning error and navigation time of 2.4 mm and 75s, respectively. The presented approach offers a versatile strategy for developing compact continuum robots for endoluminal interventions.**

***Index Terms*—Continuum Robot, Tendon-Driven, Multi-Segment, Spring Backbone, Bronchoscopy.**

I. Introduction

BRONCHOSCOPY is a critical procedure for the diagnosis and treatment of pulmonary diseases, such as lung cancer [1], [2]. Conventional rigid and flexible bronchoscopes remain standard clinical tools, but their limited dexterity and reach can hinder access to peripheral lesions in tortuous airways [3]. This challenge has motivated the development of robotic platforms that can enhance navigation, provide stability for interventions, and offer improved visualization in complex anatomical regions [4], [5].

Continuum robots (CRs) have emerged as a promising solution to these challenges, offering high dexterity and flexibility for navigation in constrained environments [6], [7]. Unlike rigid-link robots, CRs can mimic the continuous shapes and smooth motions of biological structures such as tentacles or tongues, making them suitable for medical tasks [6]. Their designs have been applied to various medical areas, including minimally invasive surgery [8], [9], endovascular interventions [10], [11], and endoscopic and endoscopically deployable robots [12], [13]. Recent advances have led to the development of robotic-assisted bronchoscopy (RAB) systems such as the Ion platform (Intuitive Surgical), Monarch (Auris Health), and the Galaxy System (Noah Medical), which employ CR architectures to enhance reach, stability, and navigation accuracy during peripheral lung access [2], [14]. Despite their clinical success in improving bronchoscopic reach and precision, these platforms rely on mechanically complex assemblies that can increase cost and limit design adaptability, motivating development of simpler CR architectures with compact and configurable designs with support for camera and biopsy tool integration [15].

Several recent developments have explored soft robotic approaches for RAB. Some target replacement of the entire bronchoscope, with fully soft or untethered platforms capable of bronchial tree navigation through approaches including magnetic-fluidic locomotion [16] or localized pneumatic anchoring [17]. In contrast, other approaches have been designed for deployment via the working channel of conventional bronchoscopes to support deeper access into distal airways. Approaches have included pneumatically actuated soft manipulators [4] and magnetically actuated catheters [18], [19]. While these soft robotic designs offer enhanced compliance for atraumatic interaction with delicate airway tissue, their fully

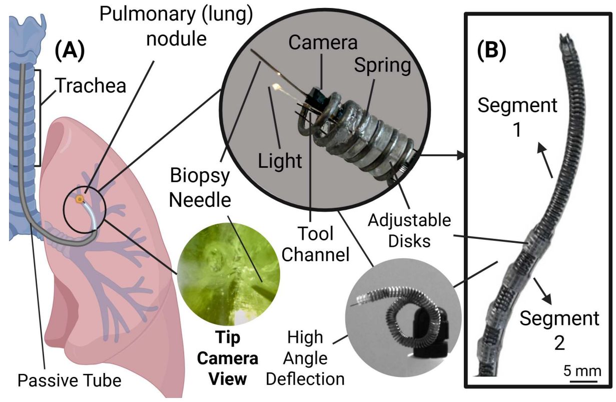

Fig. 1. (A) Illustration of the proposed spring-based TDCR navigating the bronchial tree to a distal pulmonary nodule; enlarged view highlights the compact spring–disk architecture and central tool channel with camera, light source, and biopsy needle. Inserts show camera view of biopsy needle deployment and a single-segment design under high deflection. (B) The two-segment, seven-tendon prototype, demonstrating modular spring-disk configurations.

This work was supported in part by the Engineering and Physical Sciences Research Council (EPSRC) under grants EP/Y037235/1, EP/V047914/1, and EP/V009818/1; and the National Institute for Health and Care Research (NIHR) Leeds Biomedical Research Centre (BRC) (NIHR203331). Any opinions, findings, and conclusions or recommendations expressed in this article are those of the authors and do not necessarily reflect the views of the EPSRC, or the NIHR. B. Ozdemir was supported by a scholarship from the Turkish Ministry of National Education, Republic of Turkiye. J. Chandler was supported by the Leverhulme Trust and the Royal Academy of Engineering under a RAEng/Leverhulme Trust Research Fellowship (LTRF-2425-21-154).

Burak Ozdemir, Pietro Valdastri, and James Chandler are with the School of Electronic and Electrical Engineering, University of Leeds, UK j.h.chandler@leeds.ac.uk

This article has been accepted for publication in IEEE/ASME Transactions on Mechatronics. This is the author's version which has not been fully edited and content may change prior to final publication. Citation information: DOI 10.1109/TMECH.2026.3694222

soft nature often limits steering precision, force transmission, and stability over extended working distances. As a result, despite recent advances in soft robotic navigation strategies, deployment via mechanically actuated, hard-bodied CRs or conventional bronchoscopes remains a more practical and versatile solution for distal navigation and tool delivery.

Among the different mechanical actuation strategies proposed for CRs, such as shape-memory alloys [20], concentric pre-bent interacting tubes [21], and push/pull structures [22], tendon-driven mechanisms remain particularly attractive due to their inherent compactness, high precision, and dexterity [13], [23]–[25]. However, alongside common actuation challenges associated with tendon friction, backlash and hysteresis, TD-CRs also face design constraints related to backbone integration, efficient tendon routing, and complexity of manufacture and assembly [25]. These aspects are often further exacerbated when designing TDCRs for endoluminal cases that may require compact multi-segment implementations with an open central lumen. To meet these requirements, alternative TDCR concepts featuring spring-based backbones have been introduced [26]–[28]. Clinically focused examples have included a mm-scale one-way bending surgical tool tip design [27] and a cardiac catheter capable of multi-directional bending via an assembly of spring-like 3D-printed plastic helical segments with integrated tendon-guides [28]. Although these approaches highlight the miniaturization potential and versatility of spring-like backbones, they retain trade-offs in active degrees of freedom, component material options, and design adaptability.

In the presented work we introduce a TDCR architecture and modular design framework for developing compact, configurable CRs that, for the first time, combines a spring backbone with separately fabricated self-anchoring spacer disks. With respect to existing work, our approach proposes a new architecture with the robot body and backbone formed from a continuous mechanically resilient compliant spring instead of discrete printed helical segments. We introduce self-anchoring spacer disks to provide a reconfigurable spring-disk framework for segment definition and tendon routing, while preserving a large central working channel for endoluminal imaging and tool delivery. Mechanically coupling the disks with the spring internally or externally ensures tendon alignment and provides disk stability without the need for auxiliary anchoring or separation strategies. In addition to simplified fabrication, improving design modularity can support practical reconfiguration of the robot according to procedural, anatomical and patient-specific requirements without the need for full manipulator redesign. To demonstrate the utility of the approach, we develop a two-segment TDCR configuration for RAB, featuring a three-dimensional workspace, a minimum outer diameter of 4.2 mm, and a 2.4 mm working channel housing a miniature camera, light source, and biopsy tool (Figure 1).

II. Design Approach

The presented design approach is established to provide general suitability for endoluminal applications based on three key objectives: (1) achieving a compact outer diameter, (2) preserving a large working channel for tool delivery, and (3) enabling modularity for diverse TDCR configurations. We introduce the concept of internally (Type-1) and externally (Type-2) anchored disks, considering their parametric design for independent and combined use. The proposed approach intends to support compact reconfigurable TDCR design, rather than providing a complete solution to all actuation and control challenges associated with CRs under tendon actuation.

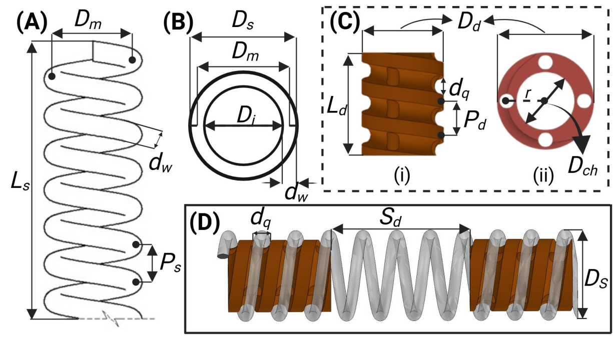

Fig. 2. The key geometric parameters defining the robot's spring-and-disk backbone. (A) Side view of the helical spring. (B) Top view defining the spring diameters. (C) The custom 3D-printed spacer disk in (i) side and (ii) top views. (D) An assembled view demonstrating the inter-disk spacing (S_d).

A. Parametric Design of the Spring-and-Disk Backbone

The fundamental structure of the robot consists of only two primary components: a helical spring that provides flexibility, and a series of internally and/or externally positioned spacer disks that define the tendon routing pathway(s) and central lumen constraints. To reduce assembly complexity and improve repeatability and robustness, the disks are designed to mechanically couple to the selected spring backbone using a *screw-in* (or *screw-on*) approach. The interaction between these elements is therefore critical and governed by geometric conditions that ensure the disk can be smoothly rotated and translated along the spring backbone during assembly, resulting in a predictable, stable, and self-anchoring engagement without the need for additional fasteners or adhesives. For the smaller internal (Type-1) disk configurations, these constraints are formalized using the key parameters illustrated in Figure 2.

To enable the disk to advance helically along the spring backbone during assembly, two fundamental geometric conditions must be satisfied. First, the disk's external (or internal) thread pitch P_d must match the spring's pitch P_s, such that:

$$P_d = P_s \tag{1}$$

Second, the groove geometry must allow the spring wire to be accommodated without interference. Assuming the Pitch Circle Diameter of the cut thread is equal to the spring's mean diameter D_m, the diameter of the groove cut into the disk d_g must be larger than the spring wire diameter d_w, such that:

$$d_g > d_w, \quad d_g = a d_w, \tag{2}$$

where a is a scaling factor to provide a clearance fit.

For Type-1 disks, the outer disk diameter D_d must be selected to lock into the spring and retain coaxial alignment

This article has been accepted for publication in IEEE/ASME Transactions on Mechatronics. This is the author's version which has not been fully edited and content may change prior to final publication. Citation information: DOI 10.1109/TMECH.2026.3694222

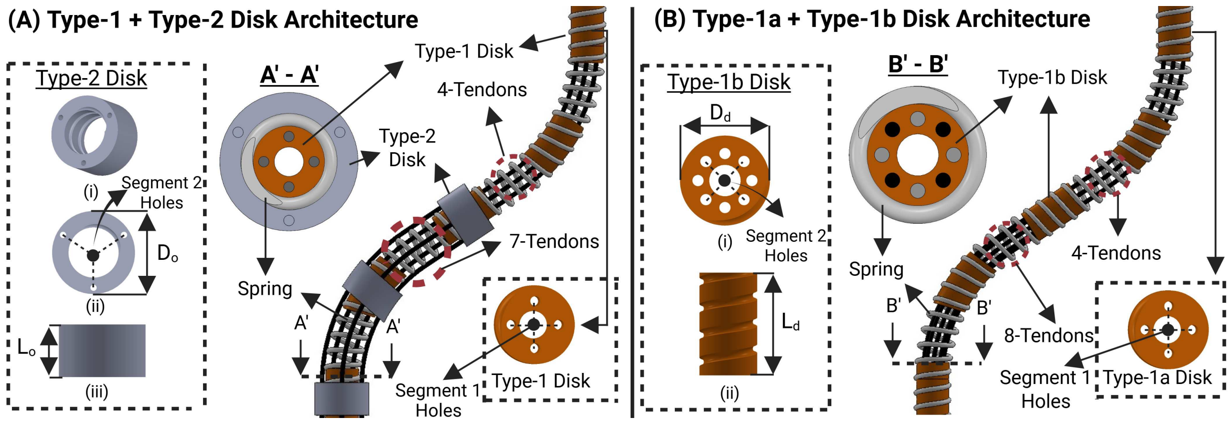

Fig. 3. Conceptualization of two distinct multi-segment architectures. (A) Utilization of both inner (Type-1) and outer (Type-2) disks, with Type-2 disks creating a proximal segment, while the Type-1 disks run the full length of the robot's backbone. (B) An alternative sequential architecture that uses two different types of internal disk (Type-1a and Type-1b) with a varying number of tendon channels to create two serially connected segments.

while supporting the optional use of externally mounted Type-2 disks. Accordingly, Type-1 disk diameters are constrained to lie between the spring's inner D_i and outer D_s diameters, and when working with Type-2 disks, are sized below the spring's mean diameter D_m via a small offset term C_d, such that:

$$D_d = D_m - C_d, \quad 0 < C_d < (D_m - D_i). \tag{3}$$

Tendon routing holes of diameter d_t must be placed on a design radius r within the inner diameter of the spring and avoiding interference with the spring wire or disk groove, as:

$$r \leq (D_i - d_t)/2 - C_r, \tag{4}$$

where C_r is a radial clearance introduced to avoid zero-thickness regions. With r defined, the maximum allowable tool channel diameter D_{ch} is determined as:

$$D_{ch} \leq 2\left(r - d_t/2 - C_t\right), \tag{5}$$

where C_t is the distance between the tendon holes and the tool channel. Additionally, the number of disks n_d with length L_d and spacing S_d must not exceed the total spring length L_s, as:

$$n_d L_d + (n_d - 1) S_d \leq L_s \tag{6}$$

Finally, the helical engagement between spacer disks and the spring backbone and the finite number of tendon routing holes introduces a specific axial resolution limit in disk placement when parallel tendon alignment is required. Axial disk separation is constrained by the spring (and disk) pitch P_d and the number of equally spaced tendon routing holes N_t, with a separation resolution Δz given by:

$$\Delta z = P_d / N_t. \tag{7}$$

Inter-disk spacing S_d is therefore governed by the geometric constraint of Eq. (6), and, when parallel tendon alignment is desired, the discrete axial spacing resolution of Eq. (7). Within these geometric constraints, S_d also serves as a design parameter governing the free spring length between adjacent disks. As such, it influences the local rigid–compliant distribution of the backbone, bending segment discretization, and structural support. The S_d value was selected to satisfy these constraints, maintain sufficient tendon-guiding support, and provide sufficient free spring lengths for high-angle bending.

B. Multi-Segment Concepts & Varied Architectures

The modular framework established can be readily extended to multi-segment designs. Figure 3 highlights two distinct multi-segment design concepts supported by the approach. In Figure 3A, both Type-1 and Type-2 spacer disks are combined. The external disks create a distinct proximal segment, while the inner disks run the full length of the robot's backbone, forming the distal segment. The second concept (Figure 3B), uses two distinct modifications of Type-1 internal disks (Type-1a and Type-1b). Additional tendon routing holes in the proximal (Type-1b) disks allow segment creation via a termination point, while allowing additional drive tendons to pass onto the distal segment. However, extending to higher segment numbers introduces constraints on disk geometry and therefore robot dimensions. Additionally, architectural trade-offs exist due to the disk types used. Type-1+Type-2 combinations are simpler for concentric multi-segment construction, where inner and outer disks define distinct segments, but require larger proximal diameters. In contrast, Type-1a+Type-1b configurations provide compact designs with simple adjustment of tendon layouts and disk placement, but can limit tool channel dimensions. As such, preferred architecture selection depends on the specific requirements of the intended CR application.

Beyond the implementations presented in Figure 3, the proposed modular design also enables further practical variation of parameters, without requiring redesign of the full manipulator. These include the segment length and number, inter-disk spacing, and tendon-routing arrangement through the selected disk types. Such parameters can influence key performance characteristics of TDCRs. For example, modifying segment length and segment and tendon number can alter the reachable workspace and dexterity profile, while changing disk spacing can adjust the local rigid-compliant distribution and bending limits. Alternative disk geometries have the potential to also support tendon arrangement variation for non-parallel and/or non-straight paths to enhance shaping or

This article has been accepted for publication in IEEE/ASME Transactions on Mechatronics. This is the author's version which has not been fully edited and content may change prior to final publication. Citation information: DOI 10.1109/TMECH.2026.3694222

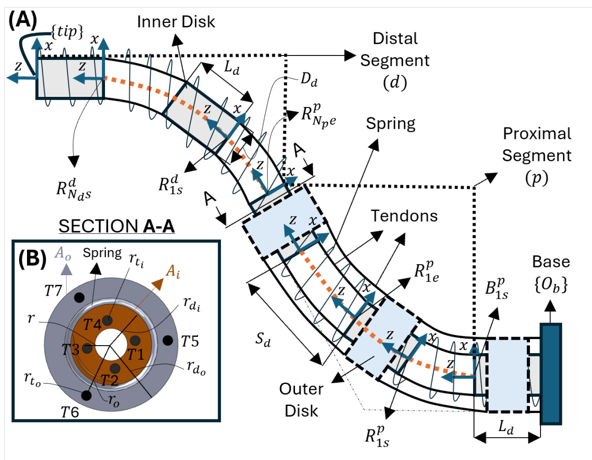

Fig. 4. Kinematic parameters of the two-segment spring-based TDCR. (A) Schematic of the proximal and distal sections, highlighting the spring-disk unit-cell structure, and local coordinate frames. (B) Cross-section (A–A) showing the tendon routing geometric parameters.

payload capabilities [29] [30]. Additionally, by parameterizing disk design based on the spring geometry, springs can be readily changed for alternative size or stiffness profiles. Overall, the design versatility and modularity provides a practical means to tune robot characteristics for different applications. For example, to suit applications requiring higher payloads or lower CR stiffness, or to provide sufficient dexterity for specific anatomical environments or intervention goals. As such, the proposed architecture should be viewed not only as a fabrication strategy, but also as a reconfigurable design platform for application-specific TDCR development.

III. Modeling

This section establishes a general kinematic modeling framework for a two-segment TDCR, considering influence of the rigid self-anchoring disks and free spring bending elements.

A. Forward Kinematics

We assume linear insertion q_{ins} is applied globally from the robot's base frame $\{O_b\}$ (Figure 4). A fixed rigid spacer disk of length L_d is located at the base before the start of the first compliant section, with the transformation from the base frame to the frame of the first proximal segment as:

$$T_{O_b}^{B_{1s}^p} = T_z(q_{\text{ins}})\, T_z(L_d), \tag{8}$$

which maps from $\{O_b\}$ to the start frame of the first proximal spring section $\{B_{1s}^p\}$. For each segment $k \in \{p, d\}$, we define local frames at the start of the spring of cell c as $\{B_{cs}^k\}$, at the start of the corresponding rigid disk as $\{R_{cs}^k\}$, and at the end of the rigid disk as $\{R_{ce}^k\}$, where c is the cell index. Each unit cell contains a spring arc of length S_d under constant-curvature bending [31], followed by a rigid spacer disk of length L_d. For segment k with curvature parameters (κ_k, ϕ_k), the spring and rigid sub-transforms are:

$$T_{B_{cs}^k}^{R_{cs}^k} = R_z(\phi_k)\, T_{\text{arc}}(\kappa_k, S_d)\, R_z(-\phi_k), \tag{9}$$

$$T_{R_{cs}^k}^{R_{ce}^k} = T_z(L_d), \tag{10}$$

Therefore, the unit-cell transform from the start of the spring to the end of the rigid disk is:

$$T_{B_{cs}^k}^{R_{ce}^k} = R_z(\phi_k)\, T_{\text{arc}}(\kappa_k, S_d)\, R_z(-\phi_k)\, T_z(L_d), \tag{11}$$

where $T_{B_{cs}^k}^{R_{ce}^k} \equiv T_{\text{cell}}^{(k)}$. The constant–curvature arc $T_{\text{arc}}(\kappa, s)$ describes the backbone position and orientation along the arc length S_d; in the straight limit we set $T_{\text{arc}}(0, S_d) = T_z(S_d)$.

Let $L_{\text{seg},k}$ denote the total length of segment k. Since each unit cell consists of a spring segment of length S_d followed by a rigid block of length L_d, the unit-cell length is $(S_d + L_d)$, and the number of full unit cells in segment k is therefore:

$$N_k = L_{\text{seg},k}/(S_d + L_d), \qquad k \in \{p, d\}. \tag{12}$$

The total transform for each segment $k \in \{p, d\}$ is computed by compounding N_k identical unit cells:

$$T_{\text{seg}}^{(k)} = \prod_{c=1}^{N_k} T_{\text{cell}}^{(k)}, \qquad k \in \{p, d\}. \tag{13}$$

As our prototype segments are contiguous, the handoff between $T_{R_{N_pe}^p}^{B_{1s}^d} = I$ is identity, where N_p is the index of the last proximal cell. Finally, the tip frame $\{t\}$ is reached by chaining the base transformation and the proximal and distal segment transforms as:

$$\boxed{T_{O_b}^{t} = \underbrace{T_{O_b}^{B_{1s}^p}}_{\text{insertion}} \cdot \underbrace{T_{\text{seg}}^{(p)}}_{\text{proximal segment}} \cdot \underbrace{T_{R_{ne}^p}^{B_{1s}^d}}_{\text{handoff}} \cdot \underbrace{T_{\text{seg}}^{(d)}}_{\text{distal segment}}} \tag{14}$$

B. Inverse Kinematics

The inverse kinematics (IK) problem aims to determine the curvature parameters (κ_p, ϕ_p) and (κ_d, ϕ_d) of the proximal and distal sections, respectively, that achieve a desired tip position $p_{\text{des}} \in \mathbb{R}^3$. Due to the nonlinear nature of the forward kinematics and the coupled effects of multiple constant-curvature sections, a closed-form solution is not pursued. Instead, a numerical IK approach is employed, where the curvature parameters are obtained by minimizing the Cartesian position error between the desired tip position and the forward kinematics prediction,

$$\min_{\boldsymbol{q}} \;\; \|p_{\text{des}} - p_{\text{tip}}(\boldsymbol{q})\|_2, \tag{15}$$

where $\boldsymbol{q} = [\kappa_p, \phi_p, \kappa_d, \phi_d]^T$ and $p_{\text{tip}}(\boldsymbol{q})$ is computed using the forward kinematics model in Section III-A, assuming a fixed insertion distance q_{ins}. The insertion motion is treated as a separately controlled degree of freedom and is not included as a decision variable in the IK optimization. The optimization was solved iteratively using a gradient-based numerical method, initialized from the previous solution to ensure continuity during motion. Specifically, the IK problem was implemented in MATLAB using the `fmincon` solver

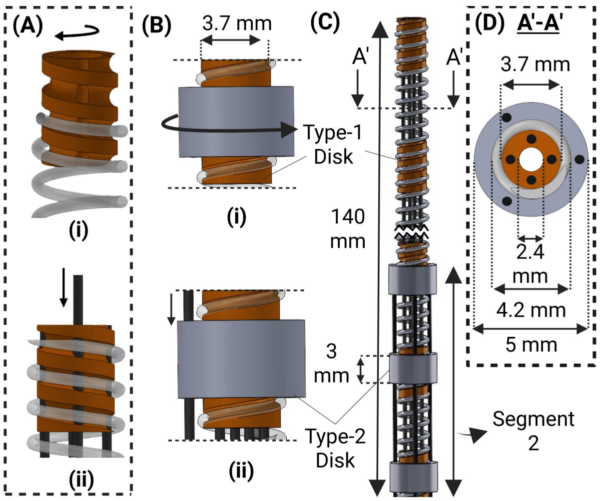

Fig. 5. Assembly overview for the multi-segment TDCR manipulators. (A) Disk assembly for the distal segment, illustrating (i) screw-in of Type-1 self-anchoring inner disks into the spring and (ii) the subsequent routing of the four inner tendons. (B) Subsequent creation of the proximal segment, showing (i) the screw-on positioning and (ii) tendon routing of a Type-2 outer disks. (C) Fully assembled 140 mm long multi-segment manipulator. (D) Cross-sectional view with concentric arrangement of Type-1 and Type-2 disks.

TABLE I
GEOMETRIC AND MATERIAL PARAMETERS OF THE ROBOT BACKBONE.

Variable	Parameter	Value
L_s	Spring total length	140 mm
$D_s\|D_m\|D_i$	Spring outer|mean|inner diameter	4.2|3.8|3.4 mm
d_w	Spring wire diameter	0.4 mm
k	Spring rate	0.149 N/mm
$D_d = 2\,r_{d_i}$	Inner disk outer diameter	3.7 mm
L_d	Inner disk length	5 mm
D_{ch}	Central channel diameter	2.4 mm
r	Inner disk tendon routing radius	1.6 mm
$D_o = 2\,r_{d_o}$	Outer disk outer diameter	5 mm
L_o	Outer disk length	3 mm
r_o	Outer disk tendon routing radius	2.3 mm
S_d	Disk spacing	10 mm
C_d	Diametral clearance ($D_m - D_d$)	0.1 mm
a	Scaling factor	1.14
$n_d\|n_o$	Number of inner|outer disks	10|5
$N_{t,i}\|N_{t,o}$	Number of inner|outer tendons	4|3
$r_{t_i}\|r_{t_o}$	Inner|outer tendon diameter	0.2|0.2 mm

with bound constraints on curvature and bending direction to enforce remaining within the feasible workspace of the robot and to avoid excessive tendon displacements. Once the desired curvature parameters are obtained, the corresponding tendon displacements are computed through the geometric relationships defined by the spring-disk architecture (see Figure 4B) using standard actuator-to-configuration relationships for three- and four-tendon arrangements [31].

IV. Fabrication and Assembly

A two-segment TDCR was developed based on the configuration of Figure 3A. Fabrication began with assembly of a single-segment manipulator with a 140 mm helical spring backbone (9637k43, McMaster-Carr) with parameters listed in Table I. Custom Type-1 disks were designed in accordance with Section II and manufactured via high-resolution stereolithography (microArch® S140, Boston Micro Fabrication) to achieve the tighter dimensional tolerances for concentric integration with Type-2 disks. The Type-1 disks were sequentially screwed into the backbone to the desired disk spacing (Figure 5A(i)). Once in place, self-anchoring removes the need for additional fixings or adhesives while allowing for future adjustment. With all Type-1 spacer disks positioned along the backbone, four 0.2 mm diameter NiTi wire actuation tendons were passed through the routing holes (Figure 5A(ii)) and fixed to the terminating distal disk with adhesive (Industrial Grade Super Glue GP). This intermediate assembly (Figure 6B(ii)) notably represents a fully functional single-segment prototype.

To realize the final two-segment manipulator, a proximal segment was created by adding Type-2 outer disks, designed based on the same spring parameters and manufactured via SLA printing (Clear v4, Form 4, Formlabs Inc.). Type-2 disks were screwed onto the proximal 60 mm of the backbone (Figure 5B(i)) and axially centered with the existing Type-1 inner disks to minimize the effective length of rigid sections along the robot's backbone (see Supplementary Video). Disks were again secured through self-anchoring and three additional 0.2 mm NiTi actuation tendons were threaded through the routing channels (Figure 5B(ii)), completing the two-segment manipulator and resulting in a seven-tendon architecture (4 inner + 3 outer tendons; Figure 5C and Figure 6B(i)).

Although realizing 3D segment motion requires only three tendons at minimum, to provide primary actuation within orthogonal planes, a four tendon arrangement was selected for the inner disks (distal segment). However, to showcase design versatility and reduce the number of actuators in the system, only three tendons were employed for the outer disks (proximal segment). This distinction also helps manage the geometric constraints of compact concentric integration, under the coupled limits of Eq. (4) and Eq. (5).

To complete the implementation for RAB, a miniature camera (ams NanEyeM) was fixed at the tip for visualization, and a fiber-based light source and a biopsy needle were deployed through the working channel for illumination and to simulate tissue sampling at predefined target locations, respectively (see Figure 1A & Supplementary Video); demonstrating the potential compatibility with standard interventional workflows in RAB. A list of these parameter values chosen for the prototype are detailed in Table I.

V. Experiments and Results

An experimental platform (Figure 6) was developed to test the 140 mm two-segment design. The robot was mounted on a fixed base with tendons routed and connected independently to miniature linear actuators (L12-100-50-12-I, Actuonix Motion Devices), each offering 100 mm stroke with integrated position feedback. Actuator control was implemented through a data acquisition system (cDAQ, National Instruments) with a custom software interface. During actuation, robot tip motion was captured via electromagnetic (EM) tracking (Aurora, Northern Digital Inc.). For planar shape analysis, a high-resolution camera (Basler aCA2040-120um) was positioned orthogonally to the robot and the recorded images post-processed (ImageJ) to extract backbone curves. Studies were subsequently conducted to assess the robot's workspace, and to evaluate kinematic model performance and navigation performance in a bronchial

This article has been accepted for publication in IEEE/ASME Transactions on Mechatronics. This is the author's version which has not been fully edited and content may change prior to final publication. Citation information: DOI 10.1109/TMECH.2026.3694222

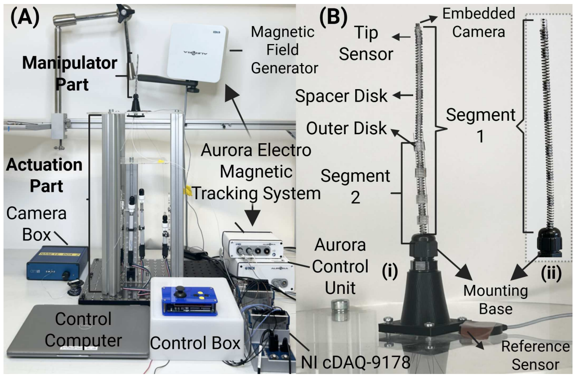

Fig. 6. The experimental setup for robot characterisation, showing (A) the manipulator, actuation unit, control hardware, and EM Tracking System, and (B) Close-up view of the (i) two- and (ii) single-segment TDCR.

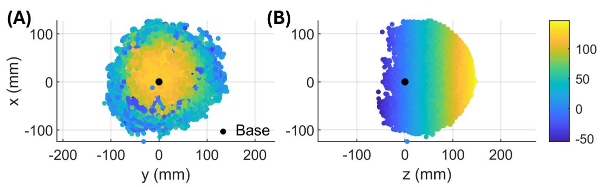

Fig. 7. Two-segment TDCR workspace characterization: (A) Top view (x–y) and (B) side view (x–z), showing ∼25,000 tracked tip positions obtained from randomized tendon actuation inputs; colorbar indicating z-axis displacement.

phantom, assessing reachability, access time, and targeting accuracy under clinically relevant conditions.

A. *Workspace Characterization*

The reachable workspace of the multi-segment TDCR was characterized by tracking the robot's distal tip position during randomized actuation. A miniature EM sensor was inserted through the central working channel and fixed at the robot tip, enabling position tracking throughout the experiments. The robot was actuated using all seven driving tendons (four inner and three outer), with a maximum of two tendons activated simultaneously. A total of approximately 25,000 tip positions were recorded from 300 randomized actuator input configurations applied within the allowable actuation limits. The resulting tip positions were recorded and projected onto the x–y and x–z planes (Figure 7). This dense sampling strategy provides a comprehensive representation of the robot's reachable workspace under practical actuation constraints.

As shown in Figure 7A, the robot exhibits a broad and well-distributed lateral workspace with near-continuous coverage around the base axis, demonstrating effective omnidirectional bending capability. The workspace boundary indicates that large curvature configurations are achievable without noticeable directional bias. In Figure 7B, the robot achieves bending configurations that reach below the base, with corresponding orientations exceeding 360° (single-segment prototype) and 310° (multi-segment prototype) (see Figure 1A and Supplemental Video). This highlights the ability of the multi-segment architecture to sustain high bending angles while maintaining stable tendon alignment and structural integrity.

B. *Planar Bending and Model Validation*

The accuracy of the proposed model was evaluated through a series of controlled tendon actuation experiments, comparing model predictions against measured tip positions and bending angles. Validation was performed using two complementary test scenarios: symmetric single-segment bending and multi-segment S-shape configurations. Figure 8 presents the results of cyclic symmetric bending experiments performed by actuating opposing tendons (Tendon 1&3) with displacement commands between 2 mm to 16 mm in 2 mm increments in increasing and decreasing directions. Figure 8A shows example images and tip bending angles during actuation.

The two opposing tendons exhibit closely matched and repeatable displacement-bending responses, with only small deviations which may be attributable to uneven tendon friction, actuator errors or due to the helical geometry of the backbone (Figure 8B). Both show clear hysteresis with loading direction indicating the influence of tendon elongation under loading, although this is minimized due to the high axial stiffness of the NiTi tendons. Figure 8C presents the corresponding measured tendon forces during displacement. Figure 8D compares the measured tip coordinates with model predictions, showing a root-mean-square error (RMSE) of 3.90 mm for Tendon 1 and 3.94 mm for Tendon 3, both within one TDCR diameter.

Beyond the displacement range evaluated in Figure 8, maximum displacement tests were conducted to evaluate assembly robustness, extreme bending range, and force transmission in blocked configurations (see Supplemental Video). The maximum measured tendon force during these tests was recorded at 20 N, which corresponded to a free bending angle of 310°, representing the maximum tip angle achieved. Under the same maximum tendon force condition, the blocked tip force was measured at representative tip configurations of 90° and 180°, yielding 1.44 N and 0.53 N, respectively.

The model was further validated under more complex multi-segment actuation S-shape configurations. Figure 9A presents images of the robot during S-shape tests, with the bending angles of the proximal and distal segments indicated. Figure 9B compares the experimentally measured full robot shape against the corresponding model predictions. The average RMSE was 4.12 mm for the tip position and 5.6 mm when considering the full shape profile, demonstrating good agreement between the model and experimental results under multi-segment bending.

C. *Phantom Navigation*

To demonstrate navigation in realistic 3D airway anatomy, experiments were conducted using a patient-specific lung phantom derived from a preoperative CT scan from the Lung Image Database Consortium (LIDC-IDRI-0807) (www.cancerimagingarchive.net). The bronchial tree was segmented using 3D Slicer to capture airways from the trachea to sub-segmental bronchi. High-resolution printing (Clear v4, Form 4, Formlabs Inc.) was used to provide a geometrically accurate environment for navigation experiments. Four navigation targets were defined, comprising two targets in the right lung (Targets 1&2) and two in the left lung (Targets 3&4), as shown in Figure 10. For each lung, targets were selected at

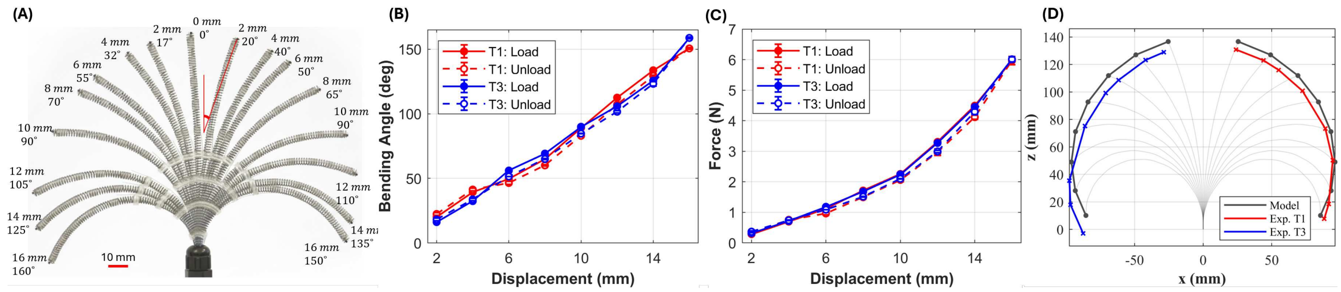

Fig. 8. Symmetric single-tendon actuation. (A) Representative bending via opposing tendon actuation (T1 and T3). (B) Measured bending angle versus tendon displacement for T1 and T3 during loading and unloading, showing the hysteresis response across three repeated trials. (C) Measured tendon force versus displacement for T1 and T3 during loading and unloading. (D) Comparison between experimental tip positions and model predictions.

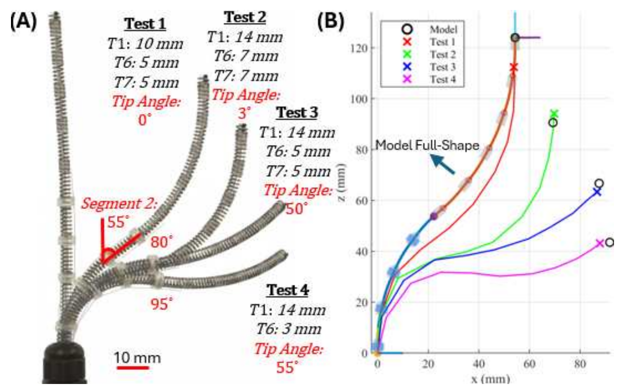

Fig. 9. Model validation for multi-segment S-shape configurations. (A) Segment-wise bending under coordinated actuation. (B) Comparison between experimentally measured full shapes of TDCR and model predictions.

the fourth (Targets 1&3) and sixth generation (Targets 2&4), resulting in four distinct navigation paths.

Navigation was performed by advancing the robot through the lung phantom using a motorized linear platform that provided controlled insertion motion. The insertion distance was treated as a known system input and updated incrementally. For each target, a navigation path was defined manually along the bronchial centerline and discretized into a sequence of intermediate waypoints. At each insertion step, the IK solver computed the bending configuration that minimized the Cartesian position error between the desired waypoint and the predicted robot tip position (mean±SD solver time 38 ± 5 ms). As such, this implementation represents waypoint-based quasi-static navigation, rather than real-time dynamic path following.

During navigation, the robot tip position was continuously tracked using an EM sensor at the robot's tip and overlaid onto the patient-specific lung geometry for visualization and analysis. The robot successfully reached all predefined target locations within the lung phantom. The average position error at the target locations was 2.35 mm across all trials. Navigation to the fourth-generation targets (Targets 1 and 3) required 71 s and 67 s, respectively, while reaching the sixth-generation targets (Targets 2 and 4) required 82 s and 79 s. Upon reaching each target location, stable deployment of a biopsy needle through the integrated working channel was demonstrated, confirming reliable tool delivery at both proximal and distal airway generations (see Supplementary Video).

VI. Conclusion

This paper presents a simplified modular design approach for the development of compact multi-segment TDCRs suited to endoluminal interventions. The proposed architecture integrates a compliant helical spring backbone with parametrically configured 3D-printed spacer disks. We present a two-segment configuration suited to RAB, with a robot diameter of 4.2 mm and a 2.4 mm central working channel. However, the modular approach and parametric design framework introduced provide a foundation for future TDCR designs to be readily configured by segment length, backbone size/stiffness, tendon and disk arrangement, and degrees of actuation to suit anatomical and functional requirements of different endoluminal tasks.

Experimental validation demonstrates agreement between a simple kinematic model based on constant curvature bending assumptions and EM tracking measurements, with a mean tip error of 4.04 mm. Navigation trials in a bronchial phantom confirm the robot's ability to reach peripheral targets with reliable deployment of the biopsy needle and light source, achieving an average positioning error of 2.35 mm.

These findings highlight the potential of modular spring-based architectures as compact and versatile platforms for navigation in highly branched luminal pathways. However, the reported tip-position and phantom-targeting errors should be interpreted in the context of the robot diameter and the confined geometry of the distal bronchi. While the present results support proof-of-concept feasibility in a representative phantom environment, common TDCR characteristics remain in the form of segment-coupling, tendon friction, and hysteresis. Development of a more comprehensive model may allow compensation for these and spring-specific effects such as compression, which may become more apparent for lower-stiffness spring implementations. Although open-loop performance may prove sufficient under vision based teleoperation, closed-loop control may be explored to support task autonomy and improve clinical safety. Future implementations may extend the presented framework to consider actively movable disks, miniaturization, and non-parallel tendon routing, to further extend application suitability.

References

[1] M. Davoudi and H. G. Colt, "Bronchoscopy simulation: a brief review," *Advances in health sciences education*, vol. 14, no. 2, pp. 287–296, 2009.

This article has been accepted for publication in IEEE/ASME Transactions on Mechatronics. This is the author's version which has not been fully edited and content may change prior to final publication. Citation information: DOI 10.1109/TMECH.2026.3694222

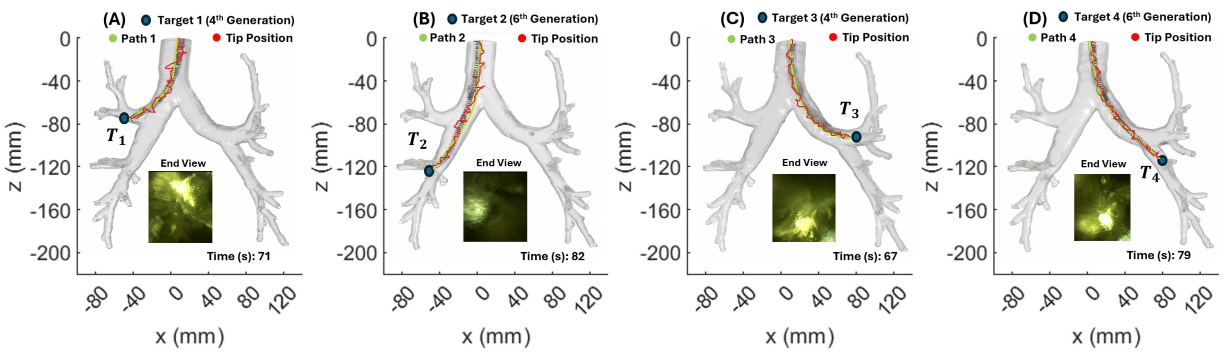

Fig. 10. Phantom navigation results in a patient-specific bronchial model, showing the robot tip positions during navigation to (A) Target 1 (right upper lung) with a positioning error of 2.18 mm, (B) Target 2 (right lower lung) with a positioning error of 2.53 mm, (C) Target 3 (left upper lung) with a positioning error of 2.24 mm, and (D) Target 4 (left lower lung) with a positioning error of 2.48 mm. Tip camera images at each target are also included.

[2] J. Puchalski, "Robotic bronchoscopy for the diagnosis of peripheral lung nodules: a review," *Current Pulmonology Reports*, vol. 10, no. 1, pp. 46–52, 2021.

[3] A. C. Chen, N. J. Pastis, M. S. Machuzak, T. R. Gildea, M. J. Simoff, C. T. Gillespie, A. K. Mahajan, S. S. Oh, and G. A. Silvestri, "Accuracy of a robotic endoscopic system in cadaver models with simulated tumor targets: Access study," *Respiration*, vol. 99, no. 1, pp. 56–61, 2020.

[4] M. McCandless, A. Perry, N. DiFilippo, A. Carroll, E. Billatos, and S. Russo, "A soft robot for peripheral lung cancer diagnosis and therapy," *Soft Robotics*, vol. 9, no. 4, pp. 754–766, 2022.

[5] Y. Li, J. Peine, M. Mencattelli, J. Wang, J. Ha, and P. E. Dupont, "A soft robotic balloon endoscope for airway procedures," *Soft Robotics*, vol. 9, no. 5, pp. 1014–1029, 2022.

[6] J. Burgner-Kahrs, D. C. Rucker, and H. Choset, "Continuum robots for medical applications: A survey," *IEEE transactions on robotics*, vol. 31, no. 6, pp. 1261–1280, 2015.

[7] T. da Veiga, J. H. Chandler, P. Lloyd, G. Pittiglio, N. J. Wilkinson, A. K. Hoshiar, R. A. Harris, and P. Valdastri, "Challenges of continuum robots in clinical context: a review," *Progress in Biomedical Engineering*, vol. 2, no. 3, p. 032003, 2020.

[8] R. E. Goldman, A. Bajo, L. S. MacLachlan, R. Pickens, S. D. Herrell, and N. Simaan, "Design and performance evaluation of a minimally invasive telerobotic platform for transurethral surveillance and intervention," *IEEE Transactions on Biomedical Engineering*, vol. 60, no. 4, pp. 918–925, 2013.

[9] M. Rox, D. S. Esser, M. E. Smith, T. E. Ertop, M. Emerson, F. Maldonado, E. A. Gillaspie, A. Kuntz, and R. J. Webster, "Toward continuum robot tentacles for lung interventions: Exploring folding support disks," *IEEE Robotics and Automation Letters*, vol. 8, no. 6, pp. 3494–3501, 2023.

[10] C. Heunis, J. Sikorski, and S. Misra, "Flexible instruments for endovascular interventions: Improved magnetic steering, actuation, and image-guided surgical instruments," *IEEE robotics & automation magazine*, vol. 25, no. 3, pp. 71–82, 2018.

[11] S. Jeon, A. K. Hoshiar, K. Kim, S. Lee, E. Kim, S. Lee, J.-y. Kim, B. J. Nelson, H.-J. Cha, B.-J. Yi *et al.*, "A magnetically controlled soft microrobot steering a guidewire in a three-dimensional phantom vascular network," *Soft robotics*, vol. 6, no. 1, pp. 54–68, 2019.

[12] J. Zhao, X. Zheng, M. Zheng, A. J. Shih, and K. Xu, "An endoscopic continuum testbed for finalizing system characteristics of a surgical robot for notes procedures," in *2013 IEEE/ASME international conference on advanced intelligent mechatronics*. IEEE, 2013, pp. 63–70.

[13] A. Kuntz, M. Emerson, T. E. Ertop, I. Fried, M. Fu, J. Hoelscher, M. Rox, J. Akulian, E. A. Gillaspie, Y. Z. Lee, F. Maldonado, R. J. Webster, and R. Alterovitz, "Autonomous medical needle steering in vivo," *Science Robotics*, vol. 8, no. 82, p. eadf7614, 2023.

[14] R. M. G. Prado, J. Cicenia, and F. A. Almeida, "Robotic-assisted bronchoscopy: A comprehensive review of system functions and analysis of outcome data," *Diagnostics*, vol. 14, no. 4, 2024.

[15] M. J. Diddams and H. J. Lee, "Robotic bronchoscopy: Review of three systems," *Life*, vol. 13, no. 2, 2023.

[16] J. Davy, T. P. Dean, N. J. Greenidge, B. Calmé, P. Lloyd, J. H. Chandler, and P. Valdastri, "Magnetic fluid-driven vine robots for minimally invasive tissue biopsy sampling," *Advanced Intelligent Systems*, p. 2400827, 2025.

[17] D. Van Lewen, T. Janke, H. Lee, R. Austin, E. Billatos, and S. Russo, "A millimeter-scale soft robot for tissue biopsy procedures," *Advanced Intelligent Systems*, vol. 5, no. 5, p. 2200326, 2023.

[18] J. Zhang, L. Liu, P. Xiang, Q. Fang, X. Nie, H. Ma, J. Hu, R. Xiong, Y. Wang, and H. Lu, "Ai co-pilot bronchoscope robot," *Nature communications*, vol. 15, no. 1, p. 241, 2024.

[19] G. Pittiglio, P. Lloyd, T. da Veiga, O. Onaizah, C. Pompili, J. H. Chandler, and P. Valdastri, "Patient-specific magnetic catheters for atraumatic autonomous endoscopy," *Soft robotics*, vol. 9, no. 6, pp. 1120–1133, 2022.

[20] C. Cheng, J. Cheng, and W. Huang, "Design and development of a novel sma actuated multi-dof soft robot," *IEEE Access*, vol. 7, pp. 75 073–75 080, 2019.

[21] H. Alfalahi, F. Renda, and C. Stefanini, "Concentric tube robots for minimally invasive surgery: Current applications and future opportunities," *IEEE Transactions on Medical Robotics and Bionics*, vol. 2, no. 3, pp. 410–424, 2020.

[22] Z. Mitros, B. Thamo, C. Bergeles, L. Da Cruz, K. Dhaliwal, and M. Khadem, "Design and modelling of a continuum robot for distal lung sampling in mechanically ventilated patients in critical care," *Frontiers in Robotics and AI*, vol. 8, p. 611866, 2021.

[23] T. Kato, I. Okumura, S.-E. Song, A. J. Golby, and N. Hata, "Tendon-driven continuum robot for endoscopic surgery: Preclinical development and validation of a tension propagation model," *IEEE/ASME Transactions on Mechatronics*, vol. 20, no. 5, pp. 2252–2263, 2014.

[24] S. Geng, Y. Wang, C. Wang, and R. Kang, "A space tendon-driven continuum robot," in *Advances in Swarm Intelligence: 9th International Conference, ICSI 2018, Shanghai, China, June 17-22, 2018, Proceedings, Part II 9*. Springer, 2018, pp. 25–35.

[25] M. Russo, S. M. H. Sadati, X. Dong, A. Mohammad, I. D. Walker, C. Bergeles, K. Xu, and D. A. Axinte, "Continuum robots: An overview," *Advanced Intelligent Systems*, vol. 5, no. 5, p. 2200367, 2023.

[26] M. Li, R. Kang, S. Geng, and E. Guglielmino, "Design and control of a tendon-driven continuum robot," *Transactions of the Institute of Measurement and Control*, vol. 40, no. 11, pp. 3263–3272, 2018.

[27] J. Wang, C. Hu, G. Ning, L. Ma, X. Zhang, and H. Liao, "A novel miniature spring-based continuum manipulator for minimally invasive surgery: Design and evaluation," *IEEE/ASME Transactions on Mechatronics*, vol. 28, no. 5, pp. 2716–2727, 2023.

[28] A. Ataollahi, R. Karim, A. S. Fallah, K. Rhode, R. Razavi, L. D. Seneviratne, T. Schaeffter, and K. Althoefer, "Three-degree-of-freedom mr-compatible multisegment cardiac catheter steering mechanism," *IEEE Transactions on Biomedical Engineering*, vol. 63, no. 11, pp. 2425–2435, 2016.

[29] M. Russo, S. Wild, X. Dong, and D. Axinte, "Helical routing: Decoupling segments of tendon-driven continuum robots," *IEEE/ASME Transactions on Mechatronics*, vol. 30, no. 3, pp. 2257–2269, 2025.

[30] K. Oliver-Butler, J. Till, and C. Rucker, "Continuum robot stiffness under external loads and prescribed tendon displacements," *IEEE Transactions on Robotics*, vol. 35, no. 2, pp. 403–419, 2019.

[31] R. J. Webster III and B. A. Jones, "Design and kinematic modeling of constant curvature continuum robots: A review," *The International Journal of Robotics Research*, vol. 29, no. 13, pp. 1661–1683, 2010.